Numerical Modelling of Hydraulic Fracturing in Cohesionless Sand: Validation Against Laboratory Experiments

Siavash Taghipoor, Alireza Nouri, and **Dave Chan,** University of Alberta

Summary

In this paper, a new hydraulic-fracturing model is introduced for cohesionless sand, which is also applicable to weak sandstone formations with high permeability and low shear strength. Phenomena such as shear-band development and shear-enhanced permeability are of paramount importance during hydraulic fracturing of cohesionless sand or weak sandstones, which make the fracturing response quite different from what it is conventionally believed to be in competent rocks.

The smeared approach in simulating hydraulic fracturing has been implemented in the proposed model within the continuum mechanics framework. Both matrix and fracture flow have been considered in this model. Tensile- and shear-fracture development and their fluid flow were simulated. The cubic law and Touhidi-Baghini's shear-permeability model (Touhidi-Baghini 1998) were used to capture the permeability evolution and to model flow in tensile and shear fractures, respectively. Shear fracturing of geomaterials involves intense localization of deformation and strain softening, which is a discontinuous phenomenon, resulting in mesh dependency of the results in the continuum model. The fracture-energy-regularization method was used in this model to reduce the mesh-size dependency of the energy dissipated during fracture propagation.

The smeared-fracture approach has been validated against laboratory hydraulic-fracturing experiments with reasonable agreement. Consistent with the experiments, the results of the numerical model indicate that tensile fractures are formed in a very small area around the injection point despite the application of high injection pressure compared with the minimum boundary stress. It is found that shear fracturing and shear-permeability evolution are the most important mechanisms that influence and control the fracturing response. The dominant fracturing mechanism is found to be governed by the high permeability and low shear strength of the material.

Introduction

Shear and tensile modes of failure, or a combination of them, have been observed in hydraulic-fracturing laboratory experiments on cohesionless sand and weak/unconsolidated sandstones (Pak 1997; Khodaverdian and McElfresh 2000; Chang 2004; Bohloli and de Pater 2006; de Pater and Dong 2007; Golovin et al. 2010; Jasarevic et al. 2010; Khodaverdian et al. 2010; Zhou et al. 2010; Olson et al. 2011). On the basis of field observations, hydraulic fractures in weak sandstone formations are different from planar two-wing fractures, as conventionally thought (Mahrer et al. 1996), and some field observations cannot be explained by classical models (Settari 1988; Weijers et al. 2000; Daneshy 2003; Onaisi et al. 2011). For instance, pressures higher than expected are usually required to fracture weak formations (Papanastasiou 1997), and field-fracture dimensions are much smaller, with widths that are much larger than predicted by existing models (Settari 1988; Weijers et al. 2000; Daneshy 2003).

The tensile mode of fracturing has been reported extensively in hydraulic-fracturing experiments (van Dam et al. 2000; Cook et al. 2004; de Pater and Dong 2007; Golovin et al. 2010; Zhou et al. 2010). Shear fracture occurs when shear stress exceeds the shear strength of the material on a discrete plane. Shear fractures and the corresponding dilation increase stresses locally, which will increase the pressure required for tensile fractures.

The majority of the current hydraulic-fracturing models assume a two-wing planar fracture, which is mostly expected in competent rocks or rocks with low permeability. However, cohesionless sand and weak/unconsolidated sandstone formations are highly permeable and prone to shear failure during pressure ramp up. Shear and tensile fractures may form a fracture network in the formation (Pak 1997; Pak and Chan 2004; Zhai 2006; Xu and Wong 2010), making the assumption of a two-wing tensile fracture with a predefined fracture direction invalid in cohesionless sand and weak/unconsolidated sandstone. Existing theories and classical models are not adequate for predicting the behaviour and growth pattern of hydraulic fractures when shear fractures and branching are involved (Settari 1988; Daneshy 2003; Osorio and Lopez 2009), and the need for new modelling approaches is evident. A numerical hydraulic-fracturing model for weak rocks should properly simulate various possible failure modes and their interaction and permeability enhancement, as well as tensile-fracture reorientation.

The smeared-fracture modelling approach enables us to simulate the potential mechanisms in the hydraulic fracturing of cohesionless sands or weak/unconsolidated sandstones. This paper presents the implementation of this approach for the numerical modelling of hydraulic fracturing on the basis of the continuum mechanics assumption. The model is validated against a large-scale hydraulic-fracturing experiment on highly permeable unconsolidated sand (Golder Associates 1992).

Failure Modes in the Hydraulic-Fracturing Process

Tensile, shear, or a mixture of the two are the common failure modes of a rock matrix during hydraulic fracturing of cohesionless sand and weak/unconsolidated sandstones. Failure has different definitions in the literature. Bieniawski et al. (1969) define failure as a change in the state of behaviour of a material whose most important types are fracture (formation of new cracks or extension of existing cracks) and rupture (disintegration of the structure into two or more pieces). Goodman (1989) describes it as a total loss of integrity of the rock, and Bésuelle et al. (2000) relate it to formation of shear band with strain-softening response. In this paper, failure refers to the peak strength of the material at which permeability starts to change significantly as a result of joining of microcracks to form macrocracks (shear or tensile band) and initiate loss of strength (strain softening). This failure forms a highly permeable zone for fluid flow, enhancing the permeability of the material.

Tensile Fracture. Tensile fracturing in hydraulic-fracturing experiments **(Fig. 1)** has been reported extensively in the literature (van Dam et al. 2000; Chang 2004; Cook et al. 2004; de Pater and Dong 2007; Golovin et al. 2010; Zhou et al. 2010). This fracture mode occurs in a single plane (two-wing planar fracture) with a predictable direction (normal to the local minimum principal stress). When more fluid is injected, the fracture grows and becomes longer in its original plane (Daneshy 2003). The fracture opening in this case is governed by the compression of the

Original SPE manuscript received for review 24 October 2013. Revised manuscript received for review 27 June 2015. Paper (SPE 178439) peer approved 26 August 2015.

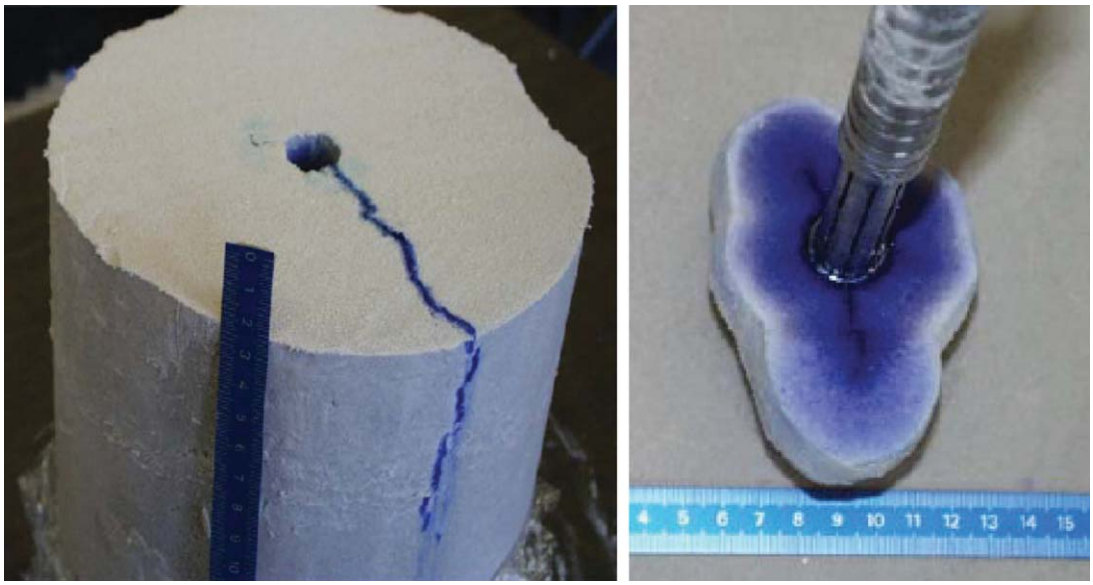

Fig. 1—Dominant tensile mode of fracturing during hydraulic fracturing (Bohloli and de Pater 2006).

material surrounding the fracture walls (Daneshy 2003). The hydraulic conductivity of a tensile fracture is a nonlinear function of the fracture opening.

Shear Fractures. Shear fracturing of the reservoir rock is very likely during injection because of the low strength of weak/unconsolidated sandstones. Shear fracturing can enhance permeability significantly as a result of shear dilation and increases local stresses around the injection zone, resulting in an increase in fracturing pressure. Shear fracturing has been related to phenomena such as multiple fracturing and fracture branching (Khodaverdian and McElfresh 2000; Daneshy 2003, 2005; Taghipoor et al. 2013).

Shear fracture in the form of subparallel fractures and multiple branching **(Fig. 2)** has been observed in hydraulic-fracturing experiments (Golder Associates 1992; Pak 1997; Khodaverdian and McElfresh 2000; Chang 2004; Bohloli and de Pater 2006; de Pater and Dong 2007; Golovin et al. 2010; Jasarevic et al. 2010; Khodaverdian et al. 2010; Zhou et al. 2010; Olson et al. 2011). In these studies, shear failure was sometimes the dominant mechanism or part of a mixed-mode fracturing. Branching and shear fracturing result in fractures shorter and narrower than predicted by existing tools (Daneshy 2003, 2005). The narrow opening causes a larger pressure drop along the fracture.

Mixed-Mode Fractures. Shear and tensile fractures may occur with some degree of interaction with each other in the process of hydraulic fracturing. **Fig. 3a** schematically illustrates the process zone ahead of the tensile-fracture tip with a high concentration of shear stresses (Papanastasiou 1997; Wu 2006).

Most hydraulic fractures in weak rocks occur in an off-balance pattern (Daneshy 2003, 2005) in which the fracture deviates from its natural plane (normal to minimum principal stress). According to Daneshy (2003), two distinct fracture characteristics are involved in off-balance growth: multiple fracturing and branching. Multiple fracturing is a near-wellbore phenomenon and refers to separate fractures created at the wellbore (Daneshy 2003), as illustrated schematically in Fig. 3b. Multiple fracturing depends on the well-completion design (e.g., borehole inclination, number, size, and distribution of perforations). However, branching depends mostly on the formation properties (Daneshy 2003).

Some field observations have been reported that cannot be explained by classical models (Settari 1988; Weijers et al. 2000; Daneshy 2003; Onaisi et al. 2011). For example, fracturing

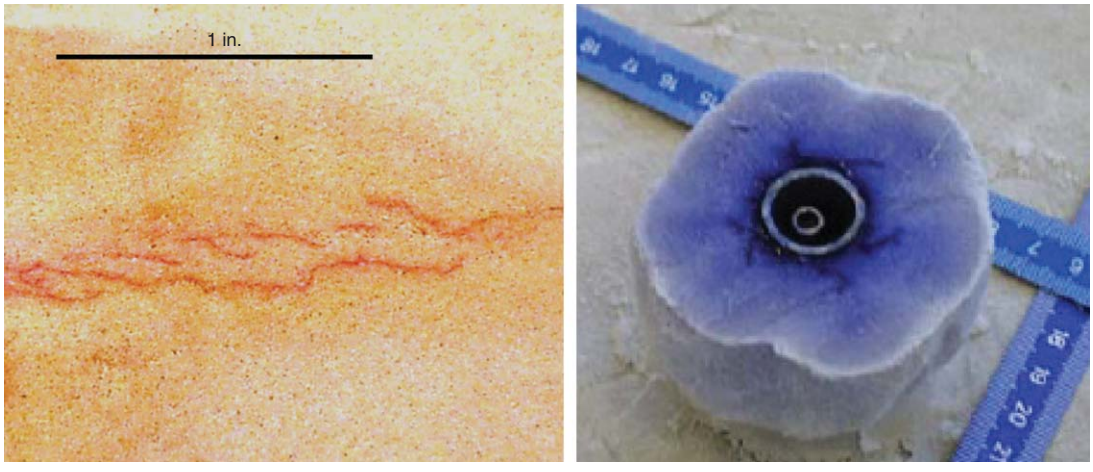

(a) (b)

Fig. 2—Shear failure during hydraulic fracturing: (a) shear and subparallel fractures during crosslink-gel injection with 35-lbm/1,000 gal polymer loading (Khodaverdian and McElfresh 2000); and (b) shear failure and multiple fracturing during injection of bentonite slurry with a concentration of 150 g/L (Bohloli and de Pater 2006).

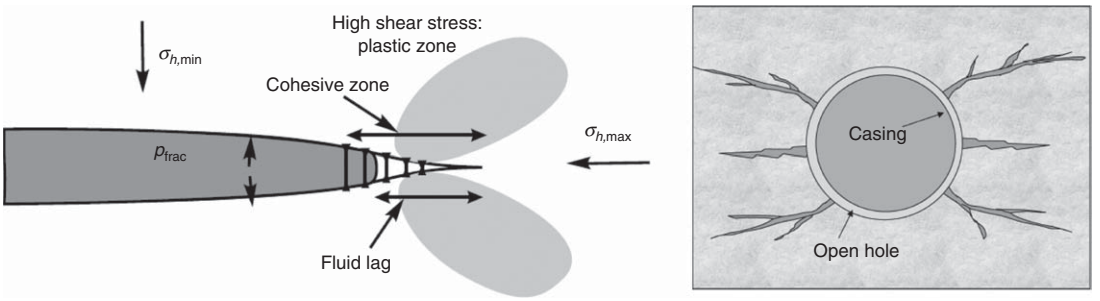

Fig. 3—(a) Shear stress concentration in the process zone ahead of the fracture tip (van Dam et al. 2000), (b) multiple fracturing near a wellbore (Daneshy 2005).

pressures are higher than both the minimum stress measured before injection and what has been calculated by models (Settari 1988; Leshchyshyn et al. 1996; Weijers et al. 2000; Daneshy 2003; Palmer et al. 2007; Osorio and Lopez 2009). A worldwide survey on fracturing pressures indicated that net pressures encountered in the field are commonly 50 to 100% higher than their corresponding values predicted by conventional fracturing simulators, which are based on linear fracture mechanics (de Pater 1996).

Pak (1997) proposed a qualitative conceptual framework for the expected hydraulic-fracture pattern in a wide range of geomaterials **(Fig. 4).** This figure relates the fracture pattern to permeability and cohesion of geomaterials. It shows that a dominant planar fracture is expected in low-permeability rocks with large cohesion, while multiple fractures are likely to occur in sandstones with lower cohesion. In highly permeable rocks with high cohesion, a rough/irregular fracture plane is expected, while for highly permeable rocks with low cohesion, a zone of tiny interconnected cracks is anticipated. The sand used in this study is located at the top right of this figure, where zones of small, interconnected fractures are expected.

Review of Numerical Models for Hydraulic Fracturing

The important mechanisms and processes in the hydraulic fracturing of weakly/unconsolidated sandstones must be considered in a numerical model (Xu and Wong 2010). These include initiation and propagation of different modes of fracture and their interaction, as well as the matrix and fracture flow. Most of the current continuum-based hydraulic-fracturing models for weakly/unconsolidated sandstones require a predetermined hydraulic-fracture direction (Papanastasiou 1997; Lian et al. 2006; Xue et al. 2006; Ji et al. 2009; Zhang et al. 2010). Even though some continuum models are adapted to capture fractures in general directions (Pak 1997; Zhai 2006; Xu 2010), they lack a proper tensile-fracture-flow law or do not simulate the development of shear bands and their interactions with the tensile fractures.

The discrete-fracture and the smeared-fracture methods are the two approaches that have been used extensively in the simulation of hydraulic fractures. In the discrete-fracture models, interface/cohesive elements are used to simulate the fractures. Some restrictions, however, are of concern in these models: (1) the logic of these programs may break down if large numbers of interfaces are included in the simulation, (2) new contacts cannot be detected automatically, and (3) the models are based on small displacements and/or rotation (Nagel et al. 2011).

A numerical tool that can capture the important phenomena involved in the hydraulic fracturing of cohesionless sand and weak/unconsolidated sandstones has yet to be developed. Multiple fractures, fracture flow, and matrix flow, as well as their deformation-dependent variations should be included in the models. This paper presents the application of the smeared-fracture approach to

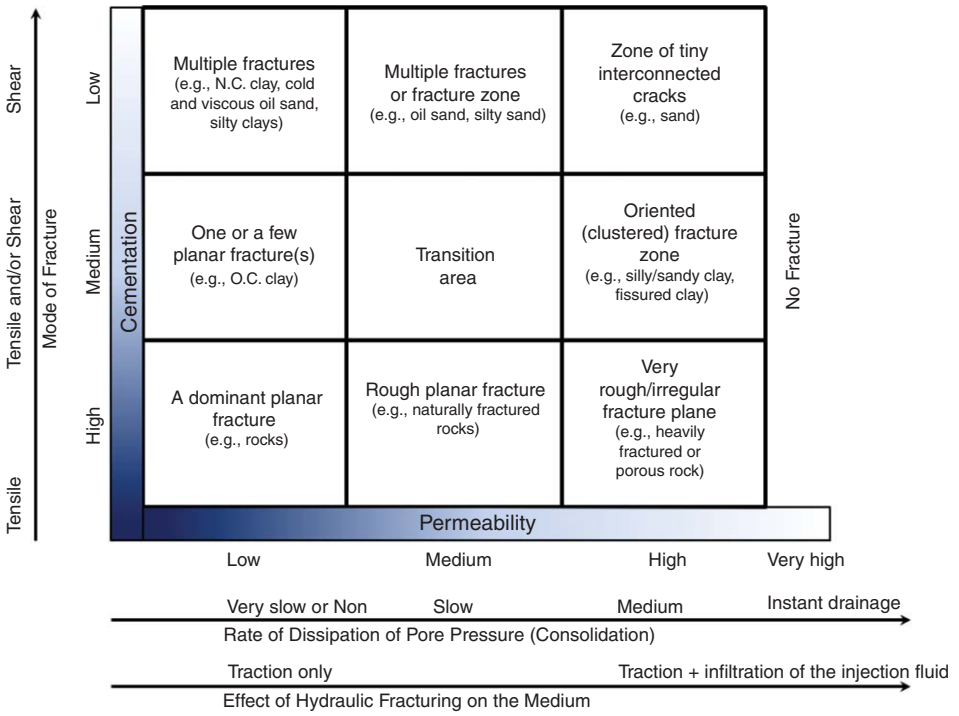

Fig. 4—Hydraulic-fracturing pattern in different geomaterials (Pak 1997).

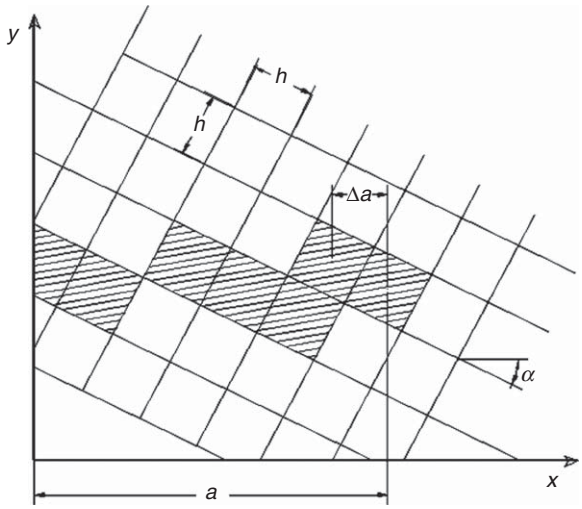

Fig. 5—Zigzag crack band with length "a" and overall direction of the crack (Bažant and Oh 1983).

the simulation of the hydraulic-fracturing process with the advantage of capturing different fracturing modes and their interaction, and the fracture and matrix fluid flow. The model is validated against laboratory experiments, as will be discussed in the following sections.

Smeared-Fracture Approach

In the smeared-fracture approach, the medium, including the fractured and unfractured rock, is treated as a continuum, and the actual stresses and strains are averaged over a certain representative volume known as the crack band. In this approach, the fracture is simulated by altering the physical and mechanical properties of the elements that satisfy the fracturing criteria. The smeared-crack model is expressed as a cracked material with equivalent anisotropic continuum properties that are degraded in the crack band (Klerck 2000).

The choice of using the discrete- or smeared-fracture approach depends on their computational effectiveness (Bažant and Oh 1983). The discrete approach involves some computational disadvantages. For instance, fracturing increases the number of nodes and changes the topological connectivity of the mesh, which creates significant challenges for automating the approach (Suidan and Schnobrich 1973; Bažant and Oh 1983). Even though the smeared-fracture approach does not fully represent the physical nature of a crack, it is an alternative to the discrete-fracture method because it enables the simulation of fracture branching, fracture rotation, and multiple shear and tensile fractures in unpredetermined directions. The smeared approach also cannot specify precisely the location of the fracture. The accuracy on the location is controlled by the size of the element. There is also the problem of mesh-size dependency unless the fracture is normalized with respect to the size of the element.

In their proposed smeared-crack approach, Bažant and Oh (1983) proposed modelling the crack band by converting the isotropic elastic moduli of the matrix to an orthotropic one, including a reduction in the stiffness in the direction perpendicular to the fracture. If a crack propagates in an arbitrary direction with respect to mesh lines or follows a curved path, it can be modelled as a zigzag crack band (see **Fig. 5**). The overall direction of this crack in the mesh approximates the actual crack direction (Bažant and Oh 1983), as shown in Fig. 5. The location of a fracture within the element cannot be captured in this approach. The smeared-fracture approach also does not account for the exact stress concentration at the fracture tip because it averages the stresses over the crack band, which is smeared over the element(s) located at the tip.

Smeared modeling of hydraulic fractures necessitates smearing both flow and mechanical properties, which are described in the following subsections.

Fluid Flow. The calculation of the equivalent permeability of shear- or tensile-fractured elements is an important challenge in smeared-fracture modeling. In some models, the equivalent permeability of a sheared matrix is estimated as a function of effective stresses (Chin and Montgomery 2004; Zhai and Sharma 2005), and the conductivity of tensile fractures is calculated on the basis of fracture-wall displacements (Ji et al. 2009). The procedures used in this paper are discussed in the following subsections.

Tensile-Fracture Flow. Assuming steady-state laminar flow of a Newtonian fluid between two parallel smooth plates (analogous to an ideal tensile fracture), the cubic law or parallel-plate theory can be derived from the Navier-Stokes equation (Zimmerman and Bodvarsson 1996; Waite et al. 1999; White 2011). With the assumption of an incompressible fluid and no-slip boundary condition (meaning that the fluid-velocity vector is equal to that of a solid at the solid/fluid boundary) (Zimmerman and Bodvarsson 1996; Waite et al. 1999; White 2011), the cubic law is given by:

$$Q = C\overline{w}_f{}^3 \nabla h, \quad \ldots\ldots\ldots\ldots\ldots\ldots\ldots\ldots \quad (1)$$

where Q is the flow rate, C is a constant that represents the geometry of the flow, $\overline{w}_f$ is the distance between the two plates (the fracture aperture), ∇ is the gradient operator, and h is the hydraulic head.

For linear flow (Witherspoon et al. 1980; Zimmerman and Bodvarsson 1996; Waite et al. 1999; White 2011), C can be expressed as:

$$C = \frac{\rho g \overline{w}_f}{12\mu L}, \quad \ldots\ldots\ldots\ldots\ldots\ldots\ldots\ldots \quad (2)$$

where L is the length of the fracture, μ is the fluid viscosity, ρ is the fluid density, and g is the gravitational acceleration.

For radial flow (e.g., a horizontal fracture in a vertical well) (Witherspoon et al. 1980), C can be expressed as:

$$C = \left[\frac{2\pi}{\ln(r_e/r_w)}\right]\left(\frac{\rho g}{12\mu}\right), \quad \ldots\ldots\ldots\ldots\ldots\ldots \quad (3)$$

where r_e and r_w are the radial distance to the far field boundary and wellbore radius, respectively.

Assuming that the wall shear stress τ_w in the fracture flow is constant, it can be normalized, resulting in the friction factor (White 2011):

$$f = \frac{8\tau_w}{\rho v^2} = \frac{12\mu}{\rho v \overline{w}_f} = \frac{a}{N_{\mathrm{Re}}}, \quad \ldots\ldots\ldots\ldots\ldots\ldots \quad (4)$$

and Reynolds number

$$N_{\mathrm{Re}} = \frac{\rho \upsilon D}{\mu}, \quad \ldots\ldots\ldots\ldots\ldots\ldots\ldots\ldots \quad (5)$$

where υ is fluid velocity and D is half-aperture $\left(D = \overline{w}_f/2\right)$. The constant a equals 96 (Witherspoon et al. 1980; Warpinski 1985; Aydin 2001; White 2011). Chen et al. (2009) have proposed Moody-type diagrams to find the friction coefficients of rough artificial fracture walls made of sand particles and cement.

Eq. 4 is further modified to include the influence of fracture-wall roughness (Witherspoon et al. 1980; Warpinski 1985; Aydin 2001), as follows:

$$f = \frac{a}{N_{\mathrm{Re}}} F_{\mathrm{rough}}, \quad \ldots\ldots\ldots\ldots\ldots\ldots\ldots\ldots \quad (6)$$

In this equation, F_{rough} represents the relative roughness of the fracture walls (i.e., the ratio of the asperities height to the fracture aperture). F_{rough} greater than unity represents deviation from the ideal conditions assumed in deriving Eq. 4. Lomize (1951) proposed the following equations for the roughness of the fracture walls in laminar flow for $\varepsilon/\overline{w}_f > 0.065$:

$$F_{\text{rough}} = \left[1 + 17\left(\frac{\varepsilon}{\overline{w}_f}\right)^{1.5}\right], \quad \ldots\ldots\ldots\ldots\ldots\ldots (7)$$

where ε is the height of the asperities. According to Lomize (1951), the factor 17 makes F_{rough} strongly dependent on the relative roughness of the fracture walls. By performing similar experiments, Louis (1969) proposed a similar equation, but a different coefficient. Huitt (1956), Parrish (1963), and Aydin (2001) have also described different equations for F_{rough}, which are not mentioned here.

The cubic law (Eq. 1) is now modified to include the fracture-wall roughness (Witherspoon et al. 1980; Aydin 2001):

$$Q = \frac{C}{F_{\text{rough}}}\overline{w}_f{}^3\nabla h. \quad \ldots\ldots\ldots\ldots\ldots\ldots\ldots\ldots (8)$$

The hydraulic conductivity of the fracture has been defined to be equivalent to the permeability parameter in Darcy's law for fluid flow in porous media (Zimmerman and Bodvarsson 1996). The fracture conductivity can be related to the equivalent fracture permeability, as follows:

$$k_f = \frac{\overline{w}_f{}^2}{12F_{\text{rough}}}, \quad \ldots\ldots\ldots\ldots\ldots\ldots\ldots\ldots (9)$$

where k_f is measured in squared metres.

Oron and Berkowitz (1998) suggested that the aperture should be averaged over a certain fracture length. On the basis of their experiments on water flow in fractures with wavy walls (sinusoidal, representing large-scale roughness) at small Reynolds numbers, as well as performing simulations using lattice gas automata, Waite et al. (1998, 1999) concluded that the tortuosity of the flow path and the aperture normal to the flow path should be considered in the cubic law equation. The tortuosity factor would appear in the denominator of Eq. 8 and would depend on the shape of the fracture configuration (sinusoidal in their study).

Modelling a fracture using a numerical method with the element size equal to the fracture thickness will result in a fine mesh because of the typically small aperture size compared with the model size, rendering engineering problems computationally impractical (Settari et al. 1990; Weill and Latil 1992). It has been demonstrated that a fracture can be included in much larger elements, provided that an equivalent permeability of the element is determined from the average of the matrix permeability and the fracture conductivity (Settari et al. 1990; Weill and Latil 1992; Ji 2008). Weill and Latil (1992) reported some mesh-size effect in the use of the smearing method in their simulations with element sizes of up to 10 m.

In this research, for fluid flow in a smeared tensile fracture, a slightly modified version of the procedure proposed by Ji (2008) and Ji et al. (2009) is used by implementing the tensile strain of the fractured element instead of the fracture aperture (Taghipoor et al. 2013), as shown in the following:

$$PM = 1 + \frac{1}{12F_{\text{rough}}k_m}\varepsilon_T{}^3t^2, \quad \ldots\ldots\ldots\ldots\ldots\ldots (10)$$

where ε_T is the tensile strain in the element, t is the equivalent element thickness in the direction of the tensile strain, and k_m is the matrix permeability. The permeability multiplier multiplied by the matrix permeability defines the permeability of a tensile fracture in the fracture direction. In the developed numerical model, the permeability multiplier PM, as calculated from Eq. 10, is applied to the permeability in the fracture direction when tensile failure is detected in the element, while the permeability in the direction normal to the fracture remains unchanged or follows the shear-permeability criteria (described in the following subsection) if a shear fracture has been detected. This orthotropic permeability tensor is then rotated back to the global coordinate system, resulting in the anisotropic permeability tensor for the fractured element.

Shear Fracture Flow. As discussed previously, the permeability of a rock matrix may increase as a result of the dilative rock response in the shearing process. Few permeability models have accounted for shear-enhanced permeability, including Kozeny-Carman (Das 2008) and the models presented by Tortike and Ali (1993), Touhidi-Baghini (1998), and Wong (2003), which are discussed briefly in the following.

The Kozeny-Carman equation expresses the absolute permeability as a function of porosity:

$$\frac{k}{k_0} = \left(\frac{\phi}{\phi_0}\right)^3\frac{(1-\phi_0)^2}{(1+\phi)}, \quad \ldots\ldots\ldots\ldots\ldots\ldots (11)$$

where k and ϕ are permeability and porosity, respectively, and the subscript zero denotes the initial value.

Derived from Kozeny-Carman's model, the Tortike-Ali equation relates permeability to volumetric strain, ε_v (Tortike and Ali 1993; Li and Chalaturnyk 2006), as follows:

$$\frac{k}{k_0} = \frac{(1+\varepsilon_v/\phi_0)}{(1+\varepsilon_v)}, \quad \ldots\ldots\ldots\ldots\ldots\ldots\ldots (12)$$

Li and Chalaturnyk (2006) conclude that this equation is applicable to determine the modified absolute permeability during isotropic unloading if the initial absolute permeability is greater than 1×10^{-12} m^2 (approximately 1 darcy).

On the basis of the permeability measurements during triaxial testing, Touhidi-Baghini (1998) proposed Eq. 13 for the permeability enhancement of McMurray oil sand (unconsolidated sand) because of shear dilation. The main assumption in this model is that rock-matrix permeability variation during the initial elastic contraction before and at the beginning of shearing is negligible **(Fig. 6),** and a major increase will occur during the shear-dilation phase, as illustrated schematically in Fig. 6.

$$\ln\frac{k}{k_0} = \frac{B}{\phi_0}\varepsilon_v, \quad \ldots\ldots\ldots\ldots\ldots\ldots\ldots\ldots (13)$$

The B factor may not be the same for different directions. With $B_h = 2$ and $B_v = 5$, Touhidi-Baghini (1998) obtained a good agreement with the experimental data for core plugs taken in the directions parallel and normal to the bedding plane.

On the basis of the experimental results, Wong (2003) proposed a strain-induced permeability model for deformable porous media in which the permeability is a linear function of strains. In this model, the principal permeability directions do not necessarily coincide with the principal strain directions. With the assumptions of isotropy and a linear relationship between permeabilities and strain components, only two constants are needed to characterize the new permeability (Wong 2003).

$$k_{ij} = \delta_{ij}k_{ij}{}^0 + (a-b)\delta_{ij}\varepsilon_{ij} + b\delta_{ij}\varepsilon_{ij} \quad \text{for two dimensions (e.g., plane strain)}, \quad \ldots\ldots\ldots (14)$$

where k_{ij} is the permeability matrix ("0" denotes initial permeability), ε_{ij} is the strain matrix, and $i, j = 1, 2$ are indexes for 2D analysis. Finally, a and b are calibration parameters. The constants a and $b - a$ characterize permeability variation resulting from both volumetric and shear deformation, respectively. A larger value of a compared with $b - a$ implies that permeability variation is dominated primarily by the porosity change, and the tortuosity effect is of secondary importance (Wong 2003).

Yuan and Harrison (2005) proposed a model for permeability enhancement caused by shear dilation by relating the permeability of an element of degraded rock to its volumetric strain. They assumed that because of large fracture permeability, intact rock permeability can be ignored. The main assumption in this model is that the degraded rock element with volume (V) can be considered as a unit containing two fractures in orthogonal directions with equal apertures (e), as illustrated schematically in **Fig. 7.** This assumption leads to an assumption of isotropic permeability in element scale. By applying the lubrication theory and relating

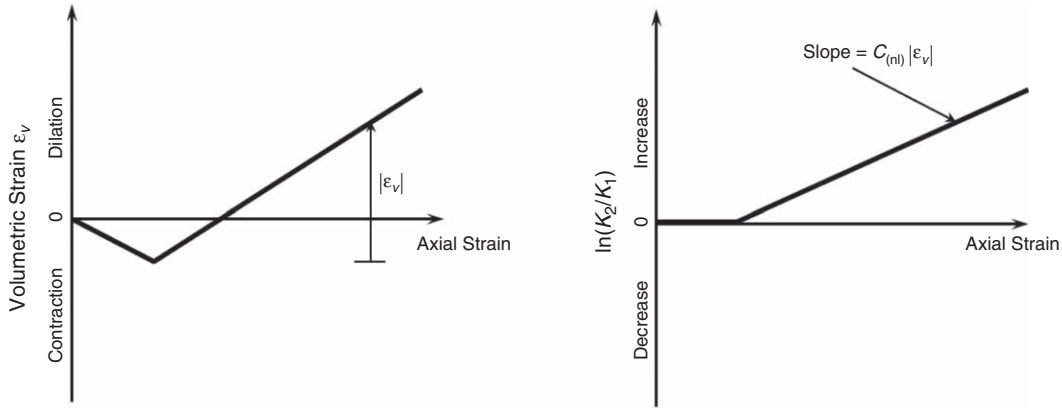

Fig. 6—Typical volumetric strain behaviour and the corresponding absolute permeability variation vs. axial strain (Touhidi-Baghini 1998).

apertures of the two fractures to the volumetric strain of the elements, as well as ignoring fracture roughness, Yuan and Harrison (2005) proposed the following relation:

$$k = \frac{e^2 g}{12\mu} = \frac{Vg}{48\mu}\varepsilon_v{}^2, \quad \ldots\ldots\ldots\ldots\ldots\ldots\ldots\ldots (15)$$

The Tortike-Ali, Kozeny-Carman, and Yuan and Harrison equations assume isotropic permeability enhancement unlike the Wong and Touhidi-Baghini models. The shear-enhanced permeability in Wong's model is a function of both shear and volumetric strain. Dilatant behaviour has been shown to be the main factor in permeability enhancement during the shearing process (Chalaturnyk 1996; Touhidi-Baghini 1998). Permeability enhancement because of shearing occurs during the dilative phase and levels off when approaching critical state. Even though the two constants (a and b) in Wong's model can be considered equal to make permeability dependent mainly on volumetric strain, the model assumes a linear relationship between volumetric strain and enhanced permeability. Conversely, Touhidi-Baghini (1998) showed that the absolute permeability of oil sand is a nonlinear function of the volumetric strain. Therefore, in this paper, Touhidi-Baghini's model in the form of Eq. 13 with different B values in the horizontal and vertical directions is used to describe the shear-permeability enhancement in hydraulic-fracturing simulations.

Darcy's law for fluid flow in 2D porous media is used for solving the flow in the intact matrix, as well as the tensile- and shear-fractured elements:

$$q_i = -\frac{k_{ij}}{\mu}\frac{\partial}{\partial x_j}\left(P - \rho_f g_k x_k\right), \quad \ldots\ldots\ldots\ldots\ldots\ldots (16)$$

where q_i is the specific discharge vector; k_{ij} is the permeability; μ is the fluid viscosity; P is the fluid pressure; ρ_f is the mass density of the fluid g_k; $k = 1, 2$ are the two components of the gravity acceleration vector; and $i, j = 1, 2$ are indices for 2D analysis.

In the developed model, porosity, permeability, and pore pressure are the variables that are exchanged between the flow and the geomechanics module in a sequentially coupled manner. For each timestep, the fluid-flow module sends the calculated pore pressures to the geomechanics module. In the geomechanics module, pore pressures are updated, and the corresponding stresses/deformations are calculated. Porosities and permeabilities are then updated on the basis of the updated strains (the cubic law for tensile-fracture permeability and the Touhidi-Baghini equation for shear permeability), which are then sent back to the fluid-flow module. This process is continued until solutions converge for the timestep. Tensile-fracture width is a solution-dependent parameter and is calculated and updated in each timestep on the basis of nodal displacements.

Treating Mesh Dependency. The post-peak behaviour of weak/unconsolidated sandstones at low effective confining stress involves intense strain localization and softening. The strain-softening behaviour of rock-type material under shear at low effective confining stress (Bažant and Oh 1983; Sulem et al. 1999; Bésuelle et al. 2000) and localization in tensile fracturing (Klerck 2000) have been investigated extensively by many researchers.

The Mohr-Coulomb plasticity model, with or without softening, does not capture the size-effect phenomenon and leads to mesh-dependent results. Therefore, a regularization technique, called fracture-energy regularization, is implemented to ensure that the energy dissipated during the formation of new fracture

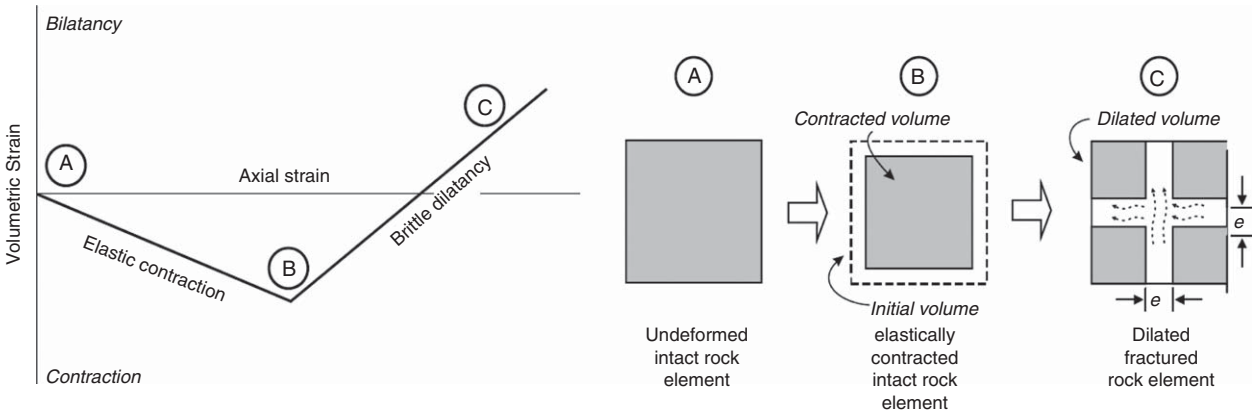

Fig. 7—Schematic of elastic compression and dilation during fracturing (Yuan and Harrison 2005).

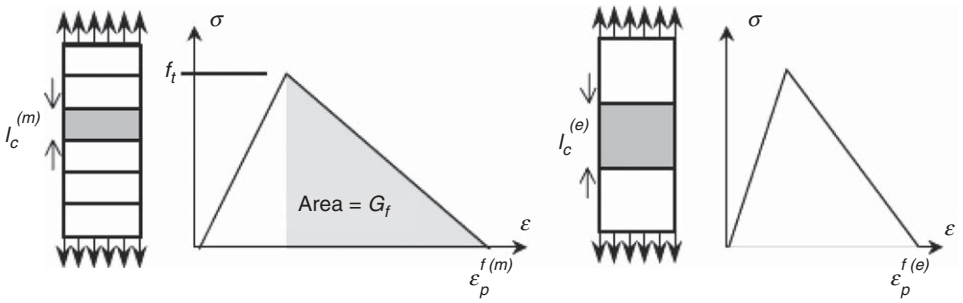

Fig. 8—Fracture-energy dissipation (Crook et al. 2003).

surfaces is mesh invariant and that the size effect is captured (Crook et al. 2003). This method is simple and straightforward to implement and is able to regularize the energy dissipated in both Mode I and Mode II fractures. For element sizes larger than the crack-band width, the fracture energy is kept constant by modifying the inelastic strain by the following equation (Crook et al. 2003):

$$g^{p(e)} = g^{p(m)} \left[\frac{l_c^{(m)}}{l_c^{(e)}} \right]^n, \quad \ldots\ldots\ldots\ldots\ldots\ldots\ldots\ldots \quad (17)$$

where $l_c^{(m)}$ is the material characteristic length equivalent to the shear/tensile band thickness (see **Fig. 8**), $l_c^{(e)}$ is the element characteristic length defined as the diameter of the circle (sphere) having equal area (volume in three dimensions) to the element under consideration, and $g^{(e)}$ and $g^{(m)}$ are inelastic fracturing strain (plastic tensile strain for Mode I fractures and plastic shear strain for Mode II fractures) of the material and element, respectively. The plastic shear strain used in this paper is the equivalent plastic strain, g^p, which is defined as (Itasca Consulting Group 2011):

$$g^p = \frac{1}{\sqrt{2}} \left[\left(\Delta e_1^{ps} - \Delta e_m^{ps} \right)^2 + \left(\Delta e_m^{ps} \right)^2 + \left(\Delta e_3^{ps} - \Delta e_m^{ps} \right)^2 \right]^{1/2} \quad \ldots\ldots\ldots\ldots\ldots\ldots\ldots\ldots (18)$$

and

$$\Delta e_m^{ps} = \frac{1}{3} \left(\Delta e_1^{ps} + \Delta e_3^{ps} \right), \quad \ldots\ldots\ldots\ldots\ldots\ldots\ldots\ldots \quad (19)$$

where Δe_m^{ps} is the volumetric plastic-shear-strain increment and Δe_j^{ps}, $(j = 1,\ 3)$ are the principal plastic-shear-strain increments. For tensile failure, g^p will be equal to the plastic-tensile-strain increment Δe_3^{pt}.

Finally, n is a material constant equal to unity with the assumption of linear elastic fracture mechanics (LEFM), which is reasonable for Mode I fractures in rock and concrete (Crook et al. 2003). Some rock types demonstrate a variable energy-release rate when fracture length changes (Bažant et al. 1993), which is best described by an *R*-curve, the material resistance to crack propagation (Anderson 1991). The behaviour of these materials deviates from the assumption of LEFM and necessitates the parameter n to depart from unity.

To implement Eq. 17, an accurate estimation of the material characteristic length, $l_c^{(m)}$ (i.e., shear band thickness), is needed. Tensile/shear degradation of weak/unconsolidated sandstones is localized in a band width, which is a function of grain size (Crook et al. 2003). The shear band thickness was selected to equal 10 times the average grain size on the basis of the work of Vardoulakis and Sulem (1995), Desai (2001), and Wolf et al. (2003).

Hydraulic-Fracturing Experiments

The hydraulic-fracturing experiments conducted by Golder Associates (1992) were used for the calibration of the smeared-hydraulic-fracture model developed in this research. A large-scale triaxial-stress chamber **(Fig. 9)** capable of containing samples of 1 m in height and 1.4 m in diameter was selected for the experiments. Dyed invert liquid sugar was used as the host fluid and injecting fluid. A steel pipe (outside diameter = 33.5 mm, inside diameter = 25.4 mm) was used as the injection well and was perforated at mid-sample height over an interval of 50 mm in eight rows of 3.5-mm-diameter holes.

Material. Lane Mountain quartz sand was used in the experiment. Small-scale laboratory tests were performed to provide flow characteristics and constitutive parameters for stress/strain behaviour of the sand. Invert liquid sugar was used as the saturating and injecting fluid, resulting in single-phase flow (Golder Associates 1992).

Testing procedure. First, the injection liner was installed, and the instrumentations for measuring sand deformation and pore-pressure transducers were suspended at a distance of one-quarter the sample radius from the wellbore at three specific levels in the sample: 100 and 250 mm above the injection level (Level 1 and 2, respectively) and 100 mm below (Level 3). At each monitoring level, two piezometers were installed at different angular positions: 90-1 and 270-1 at Level 1; 120-2 and 300-2 at Level 2; and 60-3 and 240-3 at Level 3 (the first number indicates the angular position with zero pointing south, and the second number represents the monitoring level). **Fig. 10** illustrates the layout of the instruments.

The top and bottom of the chamber were connected to a pump, allowing a constant pore pressure of 200 kPa for full saturation of the sample and drainage during the experiment. No radial drainage was allowed from the sides of the sample. The lateral and axial stresses were 400 and 600 kPa, respectively (Pak 1997). At the end of the tests, the sample was excavated in horizontal lifts (in 1.5- to 3.0-cm intervals), and the locations of the dye on the surface were marked with black strings. A photograph of the excavated surface was taken with a camera located just above the sample. By repeating this procedure for each excavation and by digitizing the photographs, a 3D fracture pattern was prepared (Pak 1997).

Results of the Experiments. The experimental results showed evidence of shear failure in the sample at all ranges of injection rate, while no dominant fracture plane was observed (Pak 1997). The dye pattern **(Fig. 11)** and the observed fractures indicated sand dilation in the sample. The dilation and the expansion constrained by the surrounding material increased the local total stresses, reducing the potential of tensile fracturing (Pak 1997). The results of the experiments in terms of pore-pressure measurements will be shown later, together with the numerical calculations. There are no available deformation measurements.

Numerical-Model Specification

The smeared-fracture methodology was implemented through the FISH functions in the FLAC software (Itasca Consulting Group 2011). The flow and stress/strain solutions were fully coupled in FLAC. The hydraulic-fracturing experiment was simulated in an axisymmetric configuration, with the axis of the wellbore as the line of symmetry.

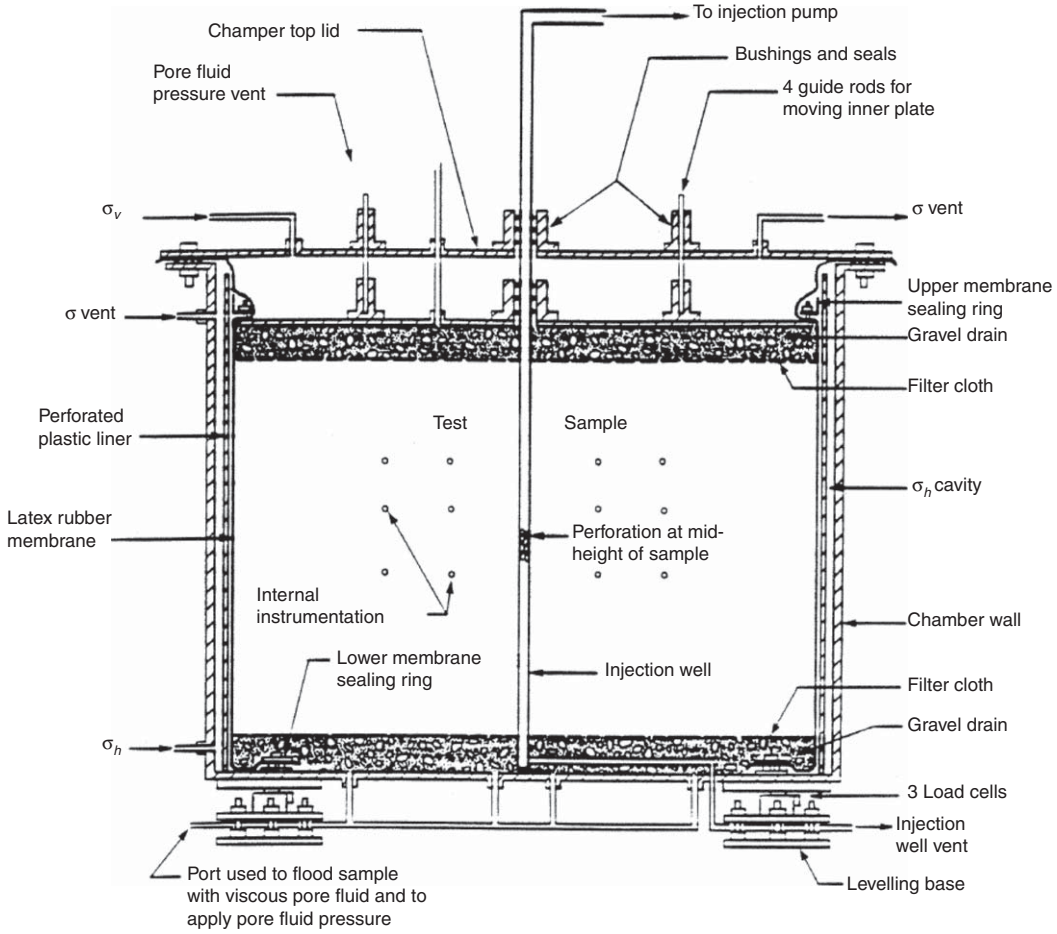

Fig. 9—Schematic cross section of the large-scale triaxial chamber used for a hydraulic-fracturing experiment (Golder Associates 1992).

Model and Grid Size. As illustrated in **Fig. 12,** a nonuniform grid was used in the numerical analysis. Three different grid sizes (9.5, 11, and 12.5 mm) were used in the perforation area to evaluate the degree of mesh dependency on the results. The model with the finest mesh is considered as the base case to study the sensitivity of the numerical results to some of the input parameters. The results of the numerical model on the 2D axisymmetric plane will be compared with the experimental results.

Initial and Boundary Condition. Normal stresses of 400 and 600 kPa were applied to the top and outer vertical boundaries, respectively. The bottom boundary and the left boundary (the

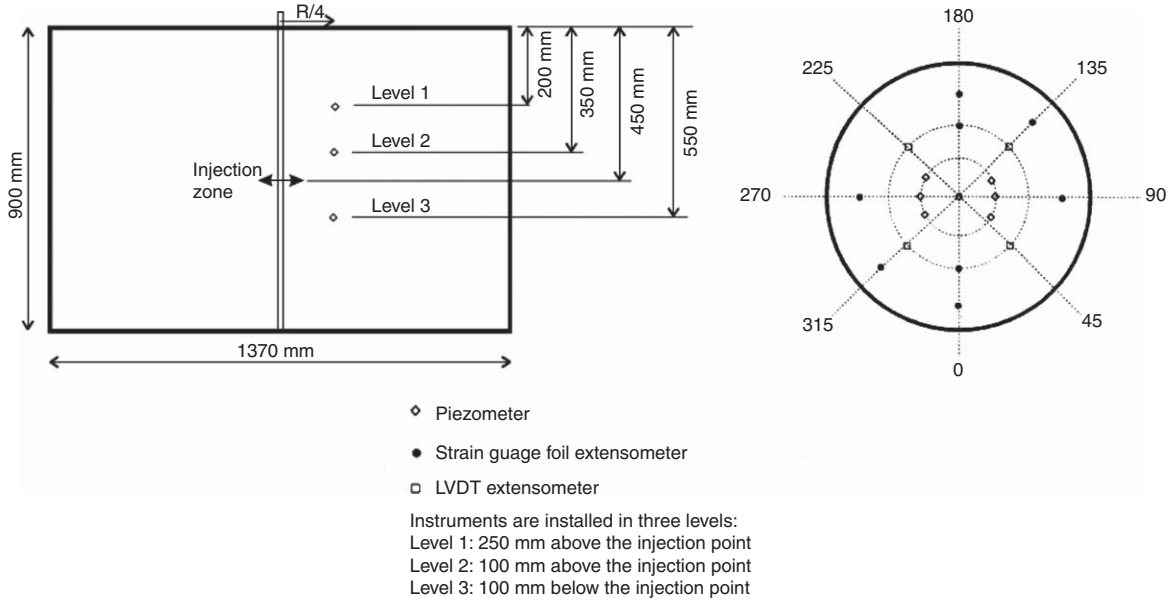

Fig. 10—Location of the piezometers for Test 4 of Phase II of the experiments (Pak 1997).

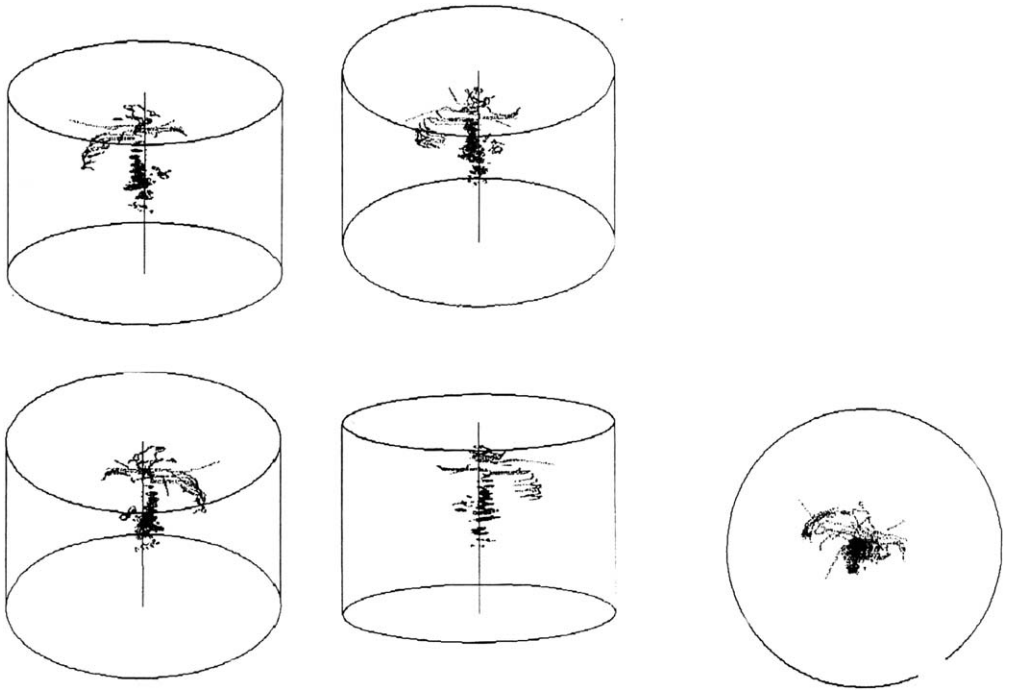

Fig. 11—Pattern of fluorescent dye in the sample (Golder Associates 1992).

liner) were fixed against displacement in the normal direction, as depicted in Fig. 11. An initial pore pressure of 200 kPa was initiated in the model. Following the initialization of the stresses and pore pressure, fluid injection was applied at the perforation interval with a constant injection rate of 30 mL/s during the experiment.

Material Properties. **Table 1** summarizes the material properties used in the simulations. The sample was cohesionless, with no tensile strength (Golder Associates 1992; Pak 1997). Peak and residual friction angles were calculated from triaxial experiments conducted on the dense Lane Mountain sand. It is assumed that the internal friction angle of the sand at peak strength declines linearly to residual friction with the accumulation of the equivalent plastic strain calculated from Eq. 18. Similarly, the peak dilation angle drops linearly to zero at full degradation.

Invert liquid sugar (injecting fluid) had a viscosity of 1.6 Pa·s, which could be reduced by adding water (5% water reduced the viscosity to 1.49 Pa·s).

During numerical calculation, every grid point was checked for tensile and shear fractures, and new permeabilities were used for tensile and shear fractures in the corresponding elements by use of Eqs. 10 and 13, respectively.

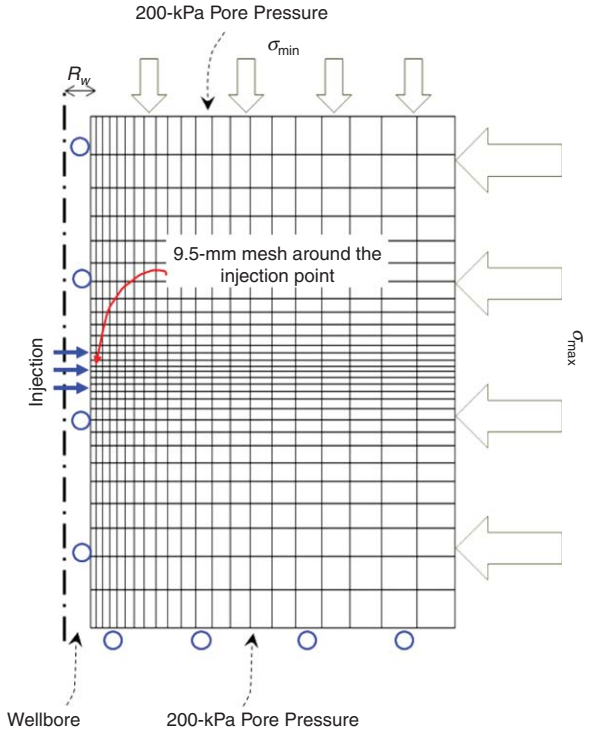

Fig. 12—Finite-difference mesh and the boundary conditions.

Validation Results

The Effect of Shear Permeability Evolution Rate. The numerical model results, in terms of pore pressure at the monitoring points, are compared with those observed in the experiment. To obtain a better match between numerical calculations and experimental measurements, different values of the B parameter were used (see Eq. 13).

Porosity (–)	0.48
Permeability (m^2)	4.48×10^{-12}
Elastic modulus (MPa)	41.05
Poisson's ratio (–)	0.25
Cohesion and tensile strength (MPa)	0
Peak friction angle	38
Residual friction angle (degrees)	30
Peak dilation angle (degrees)	38
Residual dilation angle* (degrees)	0
Average grain size (mm)	0.07
Fluid viscosity (Pa·s)	1.49
Fluid compressibility (kPa^{-1})	0.3×10^{-5}

* Assumed

Table 1—Material properties (Golder Associates 1992).

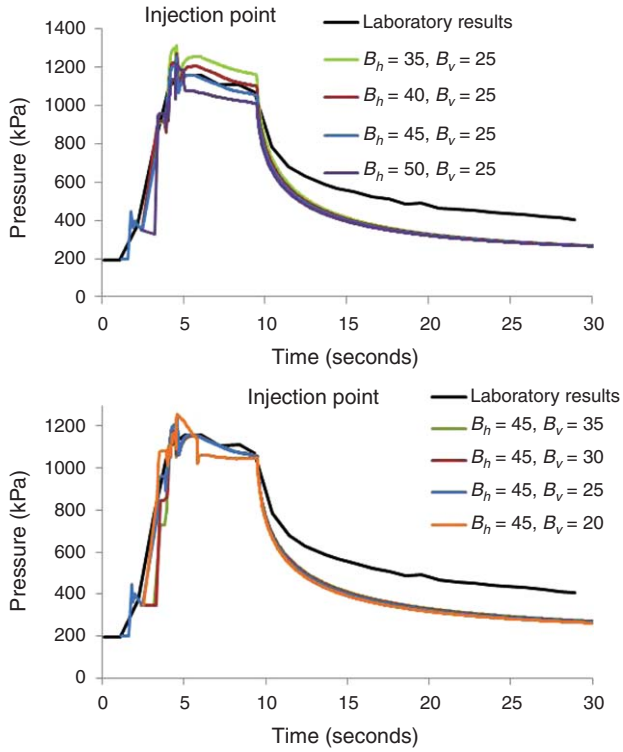

Fig. 13—Comparison of the calculated and measured pore pressure for the injection point.

Fig. 13 shows the observed and calculated pore pressures at the injection point for different B values in the vertical and horizontal directions. It can be seen that the best match corresponds to $B_h = 45$ and $B_v = 25$. A reasonable match is obtained for the pore-pressure response at this point, and the differences could be associated with the general nonsymmetric geometry of the shear fractures (Fig. 11) vs. the symmetric geometry in the numerical model. The pressure calculated for the shut-in period is lower than the experiment. It could be related to the fact that the proposed permeability is not constant for all the synthetic specimens and could vary slightly from one specimen to the other. The permeability used in the simulations is an average permeability proposed for the material. The other reason might be the assumption of axial symmetry, which assumes a symmetric fracture all around the axis of symmetry. Hydraulic fracturing is a complex phenomenon, and multiple parameters impact the geometry of the fractures, including subtle variations in material properties. A close match of the geometry of the network of shear fractures and local measurements is not expected, even for a 3D model.

Fig. 14 shows a reasonable match between the measured and the calculated pressure response at the monitoring point 90-1. The

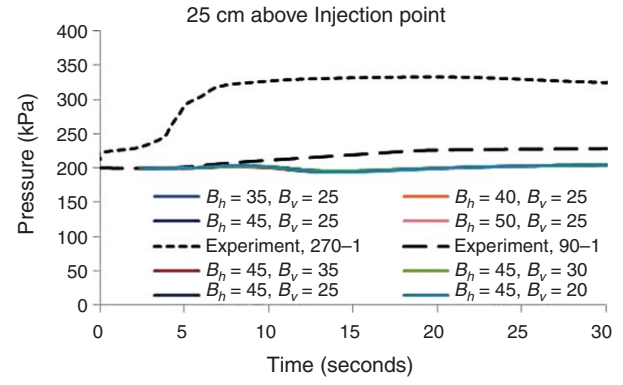

Fig. 14—Comparison of the calculated and measured pore pressure for the upper monitoring level (Level 1).

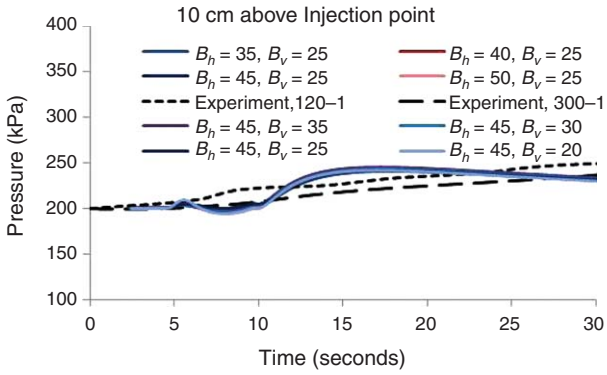

Fig. 15—Comparison of the calculated and measured pore pressure for the middle monitoring level (Level 2).

pressure profile of Point 270-1, however, is quite different than that of Point 90-1, indicating asymmetric responses at Level 1. The reason for this can be attributed to the asymmetric shear-fracture development during the injection process. It is likely that a shear band crossed the piezometer at 270-1 and increased the pore pressure at that point. Because the numerical model in an axisymmetric configuration did not allow for the capture of the asymmetric shear bands, the pore pressure at Point 270-1 was assessed to be the same at Point 90-1. Pore pressure at Level 1 was insensitive to variations in the parameters B_h and B_v, which could be related to the upward development of the shear-failure zone, which will be discussed later.

Fig. 15 shows a reasonable match between the measured and the calculated pressures at different angular positions of Level 2. The pore pressure at this monitoring level is also slightly influenced by variations in B_h and B_v. The main reason for this is believed to be the upward trend of the shear-failure zone and the localization of shear strains, which will be shown later.

Fig. 16 compares pore pressures monitored at Level 3. In the numerical model, the pressure drops to a low value of 150 kPa,

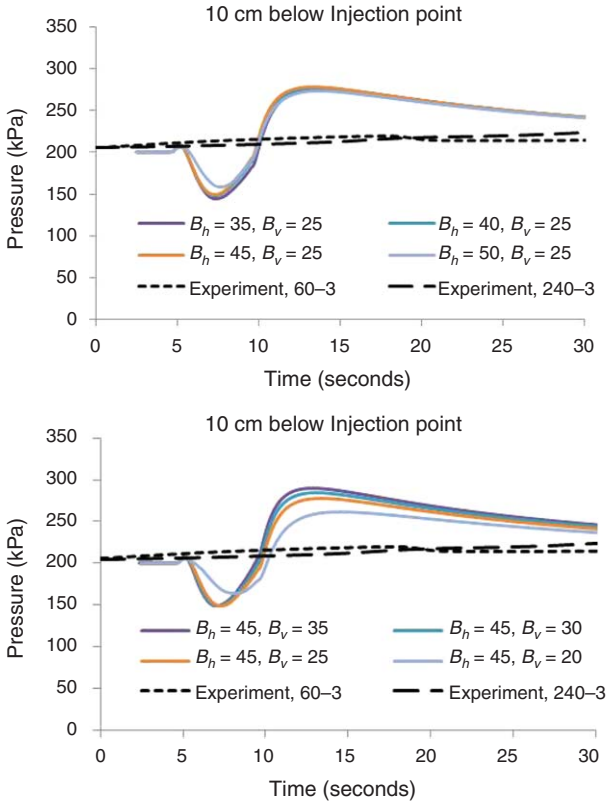

Fig. 16—Comparison of the calculated and measured pore pressure for the lower monitoring level (Level 3).

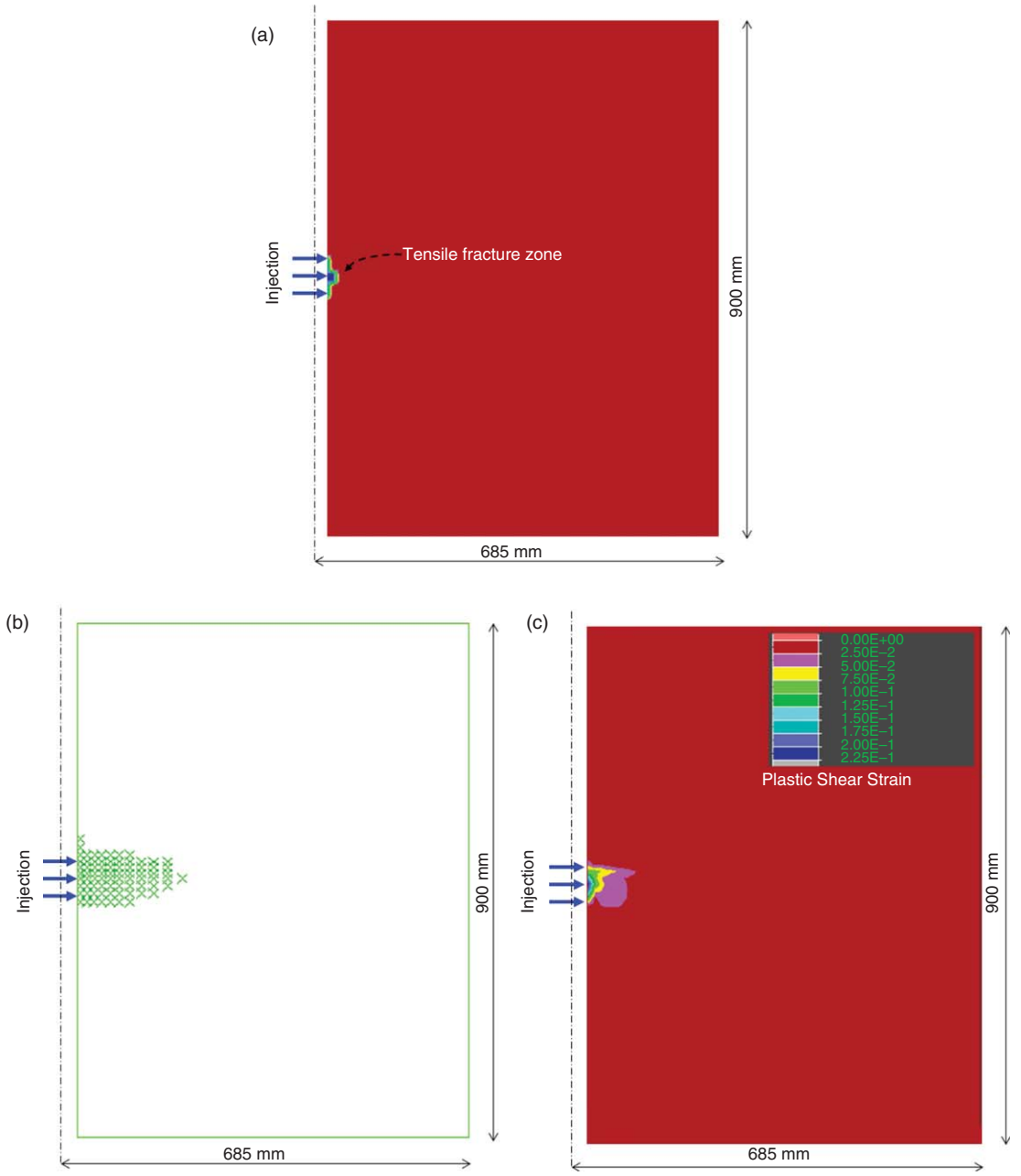

Fig. 17—(a) Size of the tensile-failure zone, (b) plastic shear strains, and (c) shear-failure zone in the numerical model.

and then rises rapidly, followed by a slight decrease. As will be shown later, the mesh size is the major contributor in this response because smaller fluctuations are obtained for the finer mesh.

The variation in the B_h parameter hardly affected the results, while a high sensitivity to the B_v magnitude is evident at this monitoring level. The smaller B_v value ($B_v = 20$) has not only reduced the fluctuation of the pore pressure, but it also has brought the pressure response closer to the measurements during the shut-in period.

Fig. 17a indicates a very small tensile-failure zone (less than 2 cm) in close vicinity to the perforations with $B_h = 45$ and $B_v = 25$, which is in line with the experimental results. Tensile failures of the same size were obtained for other B_h and B_v values. In the final report of the experimental study (Golder Associates 1992), it had been concluded that no evidence of a single dominant tensile parting or closely spaced distribution of fractures primarily normal to the initial minimum principal stress was observed in any of the fracture experiments. Permeability evolution because of shearing and diffusion of pore pressure into the sample, low shear strength, and dilative behaviour of the material are believed to be the main reasons for the inability to generate tensile fractures.

The shear-failure zone (Fig. 17b) and the plastic shear strains (Fig. 17c) are almost evenly distributed in close vicinity to the injection point at the end of the experiment, but tend to move upward after some propagation into the sample. As a result, pore-pressure diffusion tends to occur faster at the higher monitoring levels compared with the lower ones. The extent of the simulated shear zone is comparable with the observed shearing after the experiment (Fig. 11), despite the fact that the continuum model is not able to demonstrate the localized shear bands observed in the experiment.

Mesh-Size Effect. Three mesh sizes of 9.5, 11, and 12.5 mm (at the perforated interval) were used to simulate the hydraulic-fracturing experiment. The results for the three mesh sizes are illustrated in **Fig. 18.** Despite applying fracture-energy regularization to the model, the pore pressure at the mid and lower monitoring levels are significantly affected by the selected mesh size. However, the results converge toward the experimental measurements

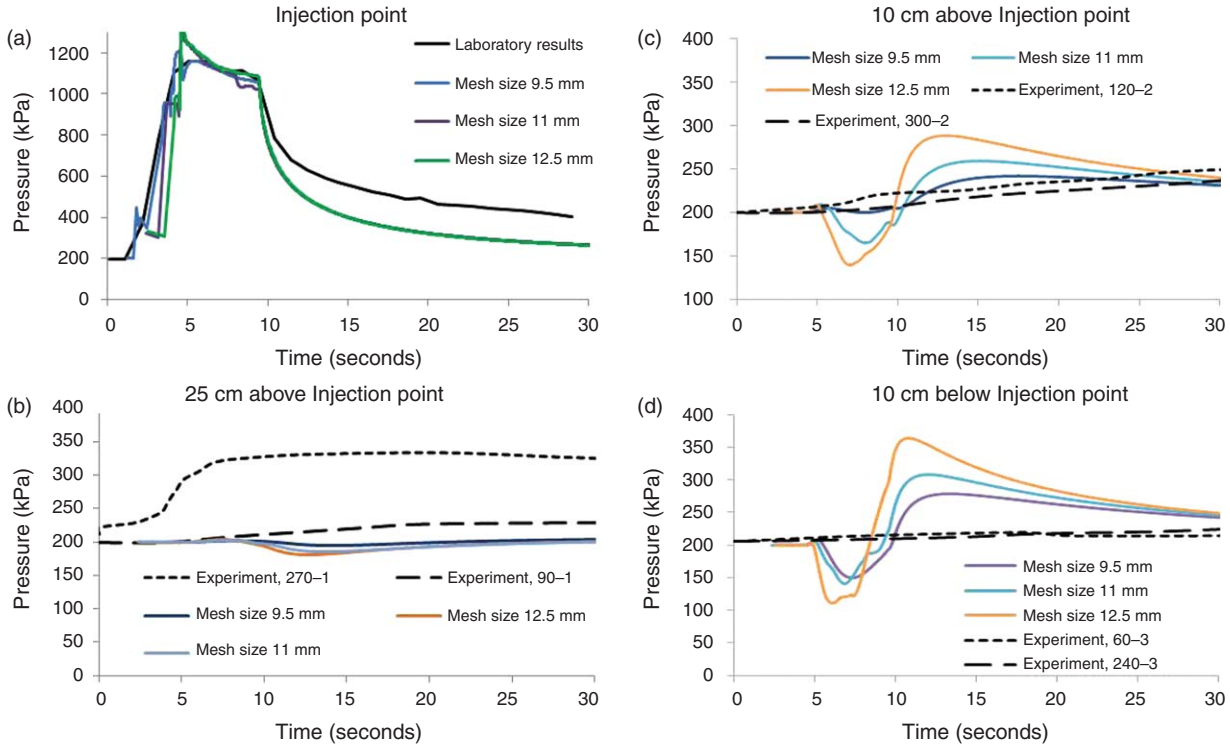

Fig. 18—Comparison between calculated and observed pore pressure vs. time for different mesh sizes.

for the finer mesh. The observed mesh dependency necessitates an examination of the effectiveness of the fracture-energy-regularization method implemented here.

To evaluate the effectiveness of the fracture-energy-regularization method, the base model has been solved without regularization. As shown in **Fig. 19,** the model without the regularization method caused larger pore pressure to build up at the injection point during the injection period (for the base case). However, no significant influence on the pore pressures inside the sample was observed. **Fig. 20** compares the degraded zone for the two models. This figure demonstrates a much larger degradation zone for the regularized model, which is closer to the experimental outcome (Fig. 11), compared with the same for the unregularized model.

Fracture-energy regularization was used to eliminate mesh dependency for stress/strain calculation, and cubic law was regularized for fracture flow on the basis of element size. It is therefore concluded that the observed mesh dependency in the results might be a result of truncation error in the explicit finite-difference scheme used in FLAC (e.g., pore pressure is averaged at the centre of the finite-difference elements). Similar mesh dependency had been observed in tensile-fracture simulations in impermeable rock, considering strain softening of tensile behaviour (Taghipoor et al. 2013).

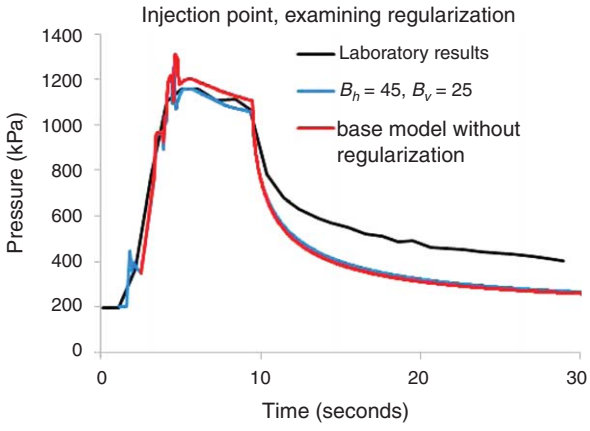

Fig. 19—Evaluating the effectiveness of fracture-energy regularization.

Summary and Conclusion

A smeared hydraulic-fracture model was developed for the simulation of hydraulic fracturing in cohesionless sand and was validated against the data from a hydraulic-fracturing experiment. Tensile- and shear-fracture conductivity were related to the deformations calculated from the constitutive response of the material.

Appropriate tensile- and shear-fracture-flow laws were implemented in the model. Reasonable agreements were obtained with the experimental outcome, especially during the injection period. The size of the tensile-fracture zone was very limited, and it was found that permeability evolution caused by shear dilation was the main contributing factor in the flow response.

Despite the use of the fracture-energy-regularization method, some mesh dependency was observed in the calculated pressures. It is believed that the truncation error in FLAC's explicit finite-difference scheme could be the main contributor. It is concluded that the smeared-fracture approach can simulate the hydraulic-fracturing process properly in cohesionless sand. It also enables simulation of the related mechanisms and processes involved, such as tensile failure and shear fracturing, shear-permeability evolution, and multiple fracturing. This model will be implemented in the investigation of field-scale hydraulic fracturing in future work.

Nomenclature

a = constant for relating friction factor to Reynolds number
a, b = constants in the Wong shear-permeability model
B_h = shear enhanced-permeability horizontal enhancement rate
B_v = shear enhanced-permeability vertical enhancement rate
C = constant representing geometry of the flow
D = fracture half-aperture, m
e = assumed fracture equal aperture
f = friction factor
F_{rough} = friction factor counting for deviation from cubic law
g_k = components of the gravity vector, m/s^2

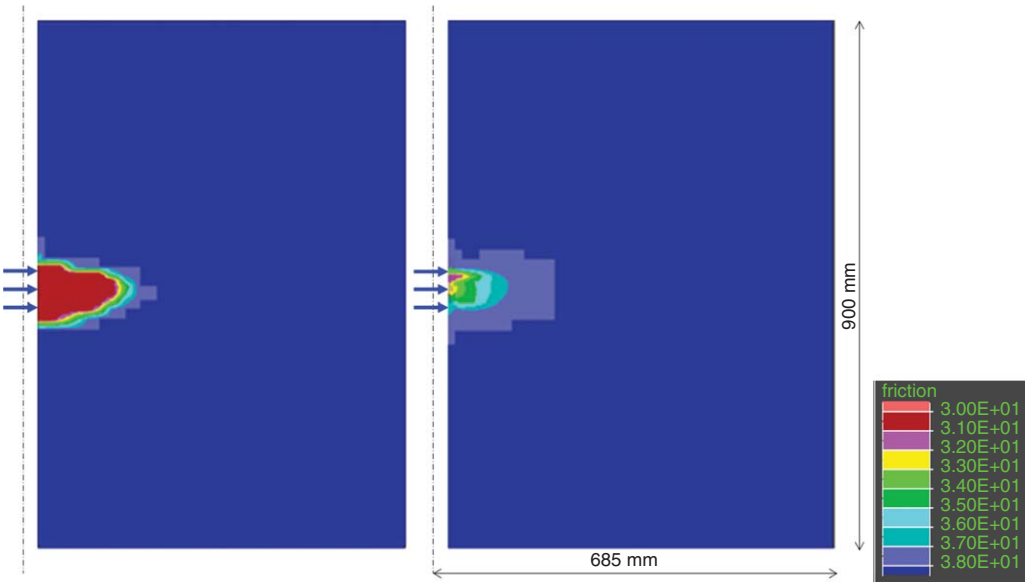

Fig. 20—Comparison of the degraded zone with and without the fracture-energy regularization in the base-case model.

g^p = equivalent plastic strain
$g^{p(e)}$ = element inelastic fracturing strain
$g^{p(m)}$ = material inelastic fracturing strain
h = hydraulic head
k = new permeability, m^2
k_0 = initial permeability, m^2
k_f = hydraulic conductivity of fracture, m^2
k_{ij} = permeability tensor, m^2
k_m = matrix permeability, m^2
$l_c^{(e)}$ = element characteristic length, m
$l_c^{(m)}$ = material characteristic length, m
L = length of the fracture, m
N_{Re} = Reynolds number
PM = permeability multiplier
q_i = specific discharge vector, m/s
Q = flow rate, m^3/s
r_e = outer radius, m
r_w = wellbore radius, m
t = element thickness, m
$\overline{w}_f$ = fracture aperture, m
W = thickness of the fracture, m
x_j = components of the coordinate system, m
Δe_j^{ps} = principal plastic-shear-strain increments
Δe_m^{ps} = volumetric plastic-shear-strain increment
ε = height of asperities, m
$\varepsilon_1, \varepsilon_3$ = principal strains
ε_T = tensile strain
ε_v = volumetric strain
ε^p = accumulated plastic shear strain
μ = fluid dynamic viscosity, Pa·s
ρ = mass density of the fluid, kg/m^3
τ_w = wall shear stress, Pa
υ = fluid kinematic velocity, m^2/s
ϕ = porosity

Acknowledgements

The authors would like to acknowledge the research funding for this study provided by the Natural Sciences and Engineering Research Council of Canada through a collaborative research development program supported by BP Canada.

References

Anderson, T. L. 1991. *Fracture Mechanics: Fundamentals and Applications*. Boca Raton, Florida: CRC Press.

Aydin, A. 2001. Fracture void structure: implications for flow, transport and deformation. *Environmental Geology* **40:** 672–677. http://dx.doi.org/10.1007/s002549900104.

Bažant, Z. P. and Oh, B. H. 1983. Crack band theory for fracture of concrete. *Matériaux et Construction* **16** (3): 155–177. http://dx.doi.org/10.1007/BF02486267.

Bažant, Z. P., Lin, F. -B., and Lippmann, H. 1993. Fracture Energy Release and Size Effect in Borehole Breakout. *International Journal for Numerical and Analytical Methods in Geomechanics* **17** (1): 1–14. http://dx.doi.org/10.1002/nag.1610170102.

Bésuelle, P., Desrues, J., and Raynaud, S. 2000. Experimental characterisation of the localisation phenomenon inside a Vosges sandstone in a triaxial cell. *International Journal of Rock Mechanics and Mining Sciences* **37** (8): 1223–1237. http://dx.doi.org/10.1016/S1365-1609(00)00057-5.

Bieniawski, Z. T., Denkhaus, H. G., and Vogler, U. W. 1969. Failure of fractured rock. *International Journal of Rock Mechanics and Mining Sciences & Geomechanics Abstracts* **6** (3): 323–341. http://dx.doi.org/10.1016/0148-9062(69)90009-6.

Bohloli, B. and de Pater, C. J. 2006. Experimental study on hydraulic fracturing of soft rocks: Influence of fluid rheology and confining stress. *Journal of Petroleum Science and Engineering* **53** (1-2): 1–12. http://dx.doi.org/10.1016/j.petrol.2006.01.009.

Chalaturnyk, R. J. 1996. *Geomechanics of the steam-assisted gravity drainage process in heavy oil reservoirs*. PhD dissertation. University of Alberta, Canada.

Chang, H. 2004. *Hydraulic Fracturing in Particulate Material*. PhD dissertation. Georgia Institute of Technology, Atlanta, Georgia (November 2004).

Chen, Z., Qian, J., Luo, S. et al. 2009. Experimental study of friction factor for groundwater flow in a single rough fracture. *Journal of Hydrodynamics, Ser. B* **21** (6): 820–825. http://dx.doi.org/10.1016/S1001-6058(08)60218-8.

Chin, L. Y. and Montgomery, C. T. 2004. A Numerical Model for Simulating Solid Waste Injection in Soft Rock Reservoirs. Presented at the SPE Annual Technical Conference and Exhibition, Houston, 26–29 September. SPE-90507-MS. http://dx.doi.org/10.2119/90507-MS.

Cook, B., Lee, M., DiGiovanni, A. et al. 2004. Discrete Element Modeling Applied to Laboratory Simulation of Near-Wellbore Mechanics. *International Journal of Geomechanics* **6** (4): 19–27. http://dx.doi.org/10.1061/(ASCE)1532-3641(2004)4:1(19).

Crook, T., Willson, S., Yu, J. G. et al. 2003. Computational modelling of the localized deformation associated with borehole breakout in quasi-brittle materials. *Journal of Petroleum Science and Engineering* **38** (3–4): 177–186. http://dx.doi.org/10.1016/S0920-4105(03)00031-7.

Daneshy, A. A. 2003. Off-Balance Growth: A New Concept in Hydraulic Fracturing. *J Pet Technol* **55** (4): 78–85. SPE-80992-JPT. http://dx.doi.org/10.2118/80992-JPT.

Daneshy, A. 2005. Proppant Distribution and Flowback in Off-Balance Hydraulic Fractures. *SPE Prod & Oper* **20** (1): 41–47. SPE-89889-PA. http://dx.doi.org/10.2118/89889-PA.

Das, B. M. 2008. *Advanced Soil Mechancis*, 3rd edition. New York, New York: Taylor and Francis.

de Pater, H. 1996. Delft Fracturing Consortium, internal presentation.

de Pater, C. J. and Dong, Y. 2007. Experimental Study of Hydraulic Fracturing in Sand as a Function of Stress and Fluid Rheology. Presented at the SPE Hydraulic Fracturing Technology Conference, College Station, Texas, USA, 29–31 January. SPE-105620-MS. http://dx.doi.org/10.2118/105620-MS.

Desai, C. S. 2001. *Mechanics of Materials and Interfaces: The Disturbed State Concept*. Boca Raton, Florida: CRC Press.

Golder Associates. 1992. Laboratory Simulation and Constitutive Behavior for Hydraulic Fracture Propagation in Oil Sands, Phase II. Final Report, Project Number 912-2055, Canada Centre for Mineral and Energy Technology.

Golovin, E., Jasarevic, H., Chudnovsky, A. et al. 2010. Observation and Characterization of Hydraulic Fracture In Cohesionless Sand. Presented at the 44th U.S. Rock Mechanics Symposium and 5th U.S.-Canada Rock Mechanics Symposium, Salt Lake City, Utah, 27–30 June. ARMA10-359.

Goodman, R. E. 1989. *Introduction to Rock Mechanics*, second edition. John Wiley & Sons.

Huitt, J. L. 1956. Fluid flow in simulated fractures. *AIChE Journal* **2** (2): 259–264. http://dx.doi.org/10.1002/aic.690020224.

Itasca Consulting Group. 2011. *FLAC Fast Lagrangian Analysis of Continua: User's Guide*. Minneapolis, Minnesota: Itasca Consulting Group, Inc.

Jasarevic, H., Golovin, E., Chudnovsky, A. et al. 2010. Observation and Modeling of Hydraulic Fracture Initiation In Cohesionless Sand. Presented at the 44th U.S. Rock Mechanics Symposium and 5th U.S.-Canada Rock Mechanics Symposium, Salt Lake City, Utah, 27–30 June. ARMA-10-360.

Ji, L. 2008. *Modeling Hydraulic Fracturing Fully Coupled with Reservoir and Geomechanical Simulation*. PhD dissertation. University of Calgary, Canada.

Ji, L., Settari, A., and Sullivan, R. B. 2009. A Novel Hydraulic Fracturing Model Fully Coupled With Geomechanics and Reservoir Simulation. *SPE J*. **14** (3): 423–430. SPE-110845-PA. http://dx.doi.org/10.2118/110845-PA.

Khodaverdian, M. and McElfresh, P. 2000. Hydraulic Fracturing Stimulation in Poorly Consolidated Sand: Mechanisms and Consequences. Presented at the SPE Annual Technical Conference and Exhibition, Dallas, Texas, USA, 1–4 October. SPE-63233-MS. http://dx.doi.org/10.2118/63233-MS.

Khodaverdian, M., Sorop, T., Postif, S. et al. 2010. Polymer Flooding in Unconsolidated-Sand Formations: Fracturing and Geomechanical Considerations. *SPE Prod & Oper* **25** (2): 211–222. SPE-121840-PA. http://dx.doi.org/10.2118/121840-PA.

Klerck, P. A. 2000. *The Finite Element Modelling of Discrete Fracture in Quasi-Brittle Materials*. PhD dissertation, University of Wales, Swansea.

Leshchyshyn, T. H., Seffari, A. and Ali, S. M. F. 1996. Minifrac Analysis of Shear Parting In Alberta Reservoirs and its Impact Towards On-site Fracture Design. Presented at the Annual Technical Meeting, Calgary, 10–12 June. PETSOC-96-79. http://dx.doi.org/10.2118/96-79.

Li, P. and Chalaturnyk, R. J. 2006. Permeability Variations Associated With Shearing and Isotropic Unloading During the SAGD Process. *J Can Pet Technol* **45** (1): 54–61. PETSOC-06-01-05. http://dx.doi.org/10.2118/06-01-05.

Lian, Z. L., Wang, X. X., Wu, H. A. et al. 2006. Modeling and Simulation of Hydraulic Fracturing Propagation in Permeable Reservoirs. *Key Engineering Materials* **324-325:** 383–386. http://dx.doi.org/10.4028/www.scientific.net/KEM.324-325.383.

Lomize, G. M. 1951. *Filtratsiya v Treshchinovatykh Porodakh* (Flow in Fractured Rocks). Gosenergoizdat, Moscow, 127 pp.

Louis, C. 1969. *A Study of Groundwater Flow in Jointed Rock and Its Influence on the Stability of Rock Masses*. London: Imperial College of Science and Technology.

Mahrer, K. D., Aud, W. W., and Hansen, J. T. 1996. Far-Field Hydraulic Fracture Geometry: A Changing Paradigm. Presented at the SPE Annual Technical Conference and Exhibition, Denver, 6–9 October. SPE-36441-MS. http://dx.doi.org/10.2118/36441-MS.

Nagel, N., Gil, I., Sanchez-Nagel, M. et al. 2011. Simulating Hydraulic Fracturing in Real Fractured Rocks - Overcoming the Limits of Pseudo3D Models. Presented at the SPE Hydraulic Fracturing Technology Conference, The Woodlands, Texas, USA, 24–26 January. SPE-140480-MS. http://dx.doi.org/10.2118/140480-MS.

Olson, J. E., Holder, J., and Hosseini, S. M. 2011. Soft Rock Fracturing Geometry and Failure Mode in Lab Experiments. Presented at the SPE Hydraulic Fracturing Technology Conference, The Woodlands, Texas, USA, 24–26 January. SPE-140543-MS. http://dx.doi.org/10.2118/140543-MS.

Onaisi, A., Ochi, J., Mainguy, M. et al. 2011. Modeling Non-Matrix Flow and Seals Integrity in Soft Sand Reservoirs. Presented at the SPE European Formation Damage Conference, Noordwijk, The Netherlands, 7–10 June. SPE-144801-MS. http://dx.doi.org/10.2118/144801-MS.

Oron, A. P. and Berkowitz, B. 1998. Flow in rock fractures: The local cubic law assumption reexamined. *Water Resour. Res.* **34** (11): 2811–2825. http://dx.doi.org/10.1029/98WR02285.

Osorio, J. G. and Lopez, C. F. 2009. Geomechanical Factors Affecting the Hydraulic Fracturing Performance in a Geomechanically Complex, Tectonically Active Area in Colombia. Presented at the SPE Latin American and Caribbean Petroleum Engineering Conference, Cartagena de Indias, Colombia, 31 May–3 June. SPE-122315-MS. http://dx.doi.org/10.2118/122315-MS.

Pak, A. 1997. *Numerical Modeling of Hydraulic Fracturing*. PhD dissertation, Department of Civil and Environmental Engineering, University of Alberta, Canada.

Pak, A. and Chan, D. H. 2004. A Fully Implicit Single Phase T-H-M Fracture Model for Modelling Hydraulic Fracturing in Oil Sands. *J Can Pet Technol* **43** (6): 35–44. PETSOC-04-06-01. http://dx.doi.org/10.2118/04-06-01.

Palmer, I., Moschovidis, Z., and Cameron, J. 2007. Modeling Shear Failure and Stimulation of the Barnett Shale After Hydraulic Fracturing. Presented at the SPE Hydraulic Fracturing Technology Conference, College Station, Texas, USA, 29–31 January. SPE-106113-MS. http://dx.doi.org/10.2118/106113-MS.

Papanastasiou, P. C. 1997. A coupled elastoplastic hydraulic fracturing model. *International Journal of Rock Mechanics and Mining Sciences* **34** (3–4): 240.e1–240.e15. http://dx.doi.org/10.1016/S1365-1609(97)00132-9.

Parrish, D. R. 1963. Fluid Flow in Rough Fractures. Presented at the University of Oklahoma-SPE Production Research Symposium, Norman, Oklahoma, USA, 29–30 April. SPE-563-MS. http://dx.doi.org/10.2118/563-MS.

Settari, A. 1988. Modelling of Fracture and Deformation Processes in Oil Sands. In Proceedings of the Fourth UNITAR/UNDP International Conference on Heavy Crude and Tar Sands, Vol. **3**, 41–54.

Settari, A., Puchyr, P. J., and Bachman, R. C. 1990. Partially Decoupled Modeling of Hydraulic Fracturing Processes. *SPE Prod Eng* **5** (1): 37–44. SPE-16031-PA. http://dx.doi.org/10.2118/16031-PA.

Suidan, M. and Schnobrich, W. C. 1973. Finite Element Analysis of Reinforced Concrete. *Journal of the Structural Division* **99:** 2109–2122.

Sulem, J., Vardoulakis, I., Papamichos, E. et al. 1999. Elasto-plastic modelling of Red Wildmoor sandstone. *Mechanics of Cohesive-frictional Materials* **4** (3): 215–245. http://dx.doi.org/10.1002/(SICI)1099-1484(199905)4:3<215::AID-CFM61>3.0.CO;2-8.

Taghipoor, S., Nouri, A., Chan, D. et al. 2013. Numerical Modelling of Hydraulic Fracturing in Weakly Consolidated Sandstones Using Smeared Fracture Approach. *Canadian Energy Technology and Innovation* **1** (2): 31–41.

Tortike, W. S. and Ali, S. M. F. 1993. Reservoir Simulation Integrated With Geomechanics. *J Can Pet Technol* **32** (5): 28–37. PETSOC-93-05-02. http://dx.doi.org/10.2118/93-05-02.

Touhidi-Baghini, A. 1998. *Absolute permeability of McMurray Formation oil sands at low confining stresses*. PhD dissertation, University of Alberta, Canada.

van Dam, D. B., Papanastasiou, P., and de Pater, C. J. 2000. Impact of Rock Plasticity on Hydraulic Fracture Propagation and Closure. Presented at the SPE Annual Technical Conference and Exhibition,

Dallas, Texas, USA, 1–4 October. SPE-63172-MS. http://dx.doi.org/10.2118/63172-MS.

Vardoulakis, I. and Sulem, J. 1995. *Bifurcation Analysis in Geomechanics*. Glasgow: Blackie Academic & Professional.

Waite, M. E., Ge, S., Spetzler, H. et al. 1998. The effect of surface geometry on fracture permeability: A case study using a sinusoidal fracture. *Geophys. Res. Lett.* **25** (6): 813–816. http://dx.doi.org/10.1029/98GL00441.

Waite, M. E., Ge, S., and Spetzler, H. 1999. A new conceptual model for fluid flow in discrete fractures: An experimental and numerical study. *J. Geophys. Res.* **104** (B6): 13049–13059. http://dx.doi.org/10.1029/1998JB900035.

Warpinski, N. R. 1985. Measurement of Width and Pressure in a Propagating Hydraulic Fracture. *Society of Petroleum Engineers Journal* **25** (1): 46–54. SPE-11648-PA. http://dx.doi.org/10.2118/11648-PA.

Weijers, L., Wright, C. A., Sugiyama, H. et al. 2000. Simultaneous Propagation of Multiple Hydraulic Fractures - Evidence, Impact and Modeling Implications. Presented at the International Oil and Gas Conference and Exhibition in China, Beijing, China, 7–10 November. SPE-64772-MS. http://dx.doi.org/10.2118/64772-MS.

Weill, L. and Latil, M. 1992. Modeling Hydraulic Fractures in a Finite Difference Reservoir Simulator. In Proc., ECMOR III: 3rd European Conference on the Mathematics of Oil Recovery. Delft, The Netherlands: Delft University Press. http://dx.doi.org/10.3997/2214-4609.201411092.

White, F. M. 2011. *Fluid Mechanics*. Columbus, Ohio: McGraw-Hill.

Witherspoon, P. A., Wang, J. S. Y., Iwai, K. et al. 1980. Validity of Cubic Law for fluid flow in a deformable rock fracture. *Water Resour. Res.* **16** (6): 1016-1024. http://dx.doi.org/10.1029/WR016i006p01016.

Wolf, H., König, D., and Triantafyllidis, T. 2003. Experimental investigation of shear band patterns in granular material. *Journal of Structural Geology* **25** (8): 1229–1240. http://dx.doi.org/10.1016/S0191-8141(02)00163-3.

Wong, R. C. K. 2003. A Model for Strain-Induced Permeability Anisotropy in Deformable Granular Media. *Canadian Geotechnical Journal* **40** (1): 95–106. http://dx.doi.org/10.1139/t02-088.

Wu, R. 2006. *Some Fundamental Mechanisms of Hydraulic Fracturing*. PhD dissertation, Georgia Institute of Technology, Atlanta, Georgia (May 2006).

Xu, B. 2010. *Finite Element Simulation of Hydraulic Fracturing in Unconsolidated Sands*. PhD dissertation, University of Calgary, Canada.

Xu, B. and Wong, R. C. K. 2010. A 3D Finite Element Model for History Matching Hydraulic Fracturing in Unconsolidated Sands Formation. *J Can Pet Technol* **49** (4): 58–66. SPE-136697-PA. http://dx.doi.org/10.2118/136697-PA.

Xue, B., Wu, H. A., Wang, X. X. et al. 2006. A Three-Dimensional Finite Element Model of Hydraulic Progressive Damage. *Key Engineering Materials* **324-325:** 375–378. http://dx.doi.org/10.4028/www.scientific.net/KEM.324-325.375.

Yuan, S. C. and Harrison, J. P. 2005. Development of a hydro-mechanical local degradation approach and its application to modelling fluid flow during progressive fracturing of heterogeneous rocks. *International Journal of Rock Mechanics and Mining Sciences* **42** (7–8): 961–984. http://dx.doi.org/10.1016/j.ijrmms.2005.05.005.

Zhai, Z. 2006. *Fracturing and Fracture Reorientation in Unconsolidated Sands and Sandstones*. PhD dissertation, The University of Texas at Austin, Austin, Texas (August 2006).

Zhai, Z. and Sharma, M. M. 2005. A New Approach to Modeling Hydraulic Fractures in Unconsolidated Sands. Presented at the SPE Annual Technical Conference and Exhibition, Dallas, Texas, USA, 9–12 October. SPE-96246-MS. http://dx.doi.org/10.2118/96246-MS.

Zhang, G. M., Liu, H., Zhang, J. et al. 2010. Three-dimensional finite element simulation and parametric study for horizontal well hydraulic fracture. *Journal of Petroleum Science and Engineering* **72** (3–4): 310–317. http://dx.doi.org/10.1016/j.petrol.2010.03.032.

Zhou, J., Dong, Y., de Pater, C. J. et al. 2010. Experimental Study of the Impact of Shear Dilation and Fracture Behavior During Polymer Injection for Heavy Oil Recovery in Unconsolidated Reservoirs. Presented at the Canadian Unconventional Resources and International Petroleum Conference, Calgary, 19–21 October. SPE-137656-MS. http://dx.doi.org/10.2118/137656-MS.

Zimmerman, R. W. and Bodvarsson, G. S. 1996. Hydraulic Conductivity of Rock Fractures. *Transport in Porous Media* **23** (1): 1–30. http://dx.doi.org/10.1007/BF00145263.

Siavash Taghipoor is a senior ground control engineer and ground control supervisor at KGHM International. He has also been a PhD degree candidate in petroleum engineering at the University of Alberta, and received the Chevron Graduate Scholarship in Natural Gas Engineering at the University of Alberta in 2010. Taghipoor's research interests include numerical modelling and geomechanics. He holds an MSc degree in rock mechanics from Amirkabir University of Technology (Tehran Polytechnic) in Iran. Taghipoor has more than 8 years of industrial experience and has authored or coauthored 10 papers.

Alireza Nouri is an associate professor in the School of Mining and Petroleum Engineering, Department of Civil & Environmental Engineering at the University of Alberta. He has 5 years of industrial experience and has been involved in several years of consulting activities in such matters as sand production and hydraulic fracturing. Nouri has supervised several PhD degree students and researchers at the University of Alberta. His team is involved in research projects on topics such as numerical- and physical-model testing of sand production, numerical-model development for hydraulic fracturing, frac-pack-model development, caprock-integrity analysis of steam-assisted gravity-drainage (SAGD) projects, laboratory testing of sand control in SAGD operations, wellbore stability and breakout studies, development of models for continuous rock degradation and failure analysis, sand consolidation, and the investigation of sand liquefaction potential in injection wells under water-hammer pressure pulsing, among others. Nouri and his team have performed sand-production analysis for several oil fields in the Gulf of Mexico, Angola, and Azerbaijan. He has authored or coauthored more than 70 technical papers. Several of these publications have been in highly reputed journals, such as *SPE Journal, Journal of Canadian Petroleum Technology, Journal of Petroleum Science and Engineering,* and *International Journal of Rock Mechanics and Mining Sciences,* among others. Nouri is a registered professional engineer in Alberta and a member of SPE.

Dave Chan is currently a professor and the associate chair of Graduate Studies of Civil and Environmental Engineering at the University of Alberta. He has authored or coauthored more than 120 technical papers. Chan's current research is focused on the development of constitutive models for geomaterials and numerical methods for analyzing ground deformation and mobility. He holds a BSc degree and an MSc degree from McMaster University and a PhD degree from the University of Alberta.